Atmospheric Chemistry and Physics

3-D polarised simulations of space-borne passive mm/sub-mm midlatitude cirrus observations: a case study

C. P. Davis[1], **K. F. Evans**[2], **S. A. Buehler**[3], **D. L. Wu**[4], **and H. C. Pumphrey**[1]

[1]Institute of Atmospheric and Environmental Science, University of Edinburgh, Edinburgh, UK
[2]Dept. of Atmosphere and Oceanic Sciences, University of Colorado, Boulder, USA
[3]Department of Space Science, Lulea Technical University, Kiruna, Sweden
[4]Jet Propulsion Laboratory, California Institute of Technology, Pasadena, USA

Abstract. Global observations of ice clouds are needed to improve our understanding of their impact on earth's radiation balance and the water-cycle. Passive mm/sub-mm has some advantages compared to other space-borne cloud-ice remote sensing techniques. The physics of scattering makes forward radiative transfer modelling for such instruments challenging. This paper demonstrates the ability of a recently developed RT code, ARTS-MC, to accurately simulate observations of this type for a variety of viewing geometries corresponding to operational (AMSU-B, EOS-MLS) and proposed (CIWSIR) instruments. ARTS-MC employs an adjoint Monte-Carlo method, makes proper account of polarisation, and uses 3-D spherical geometry. The actual field of view characteristics for each instrument are also accounted for. A 3-D midlatitude cirrus scenario is used, which is derived from Chilbolton cloud radar data and a stochastic method for generating 3-D ice water content fields. These demonstration simulations clearly demonstrate the beamfilling effect, significant polarisation effects for non-spherical particles, and also a beamfilling effect with regard to polarisation.

1 Introduction

Probably the greatest uncertainty in future projections of climate arises from clouds, their interactions with radiation, and their role in the hydrological cycle. Clouds can both absorb and reflect solar radiation (thereby cooling the surface) and absorb and emit long wave radiation (thereby warming the surface) (Houghton et al., 2001). The water vapour budget of the climatically sensitive region of the upper troposphere is greatly influenced by the amount of cloud ice and its vertical distribution (Lynch et al., 2002). Improved observations

of the ice water content of clouds and the vertical distribution of these clouds are required to assess and improve the treatment of cloud/radiation interaction and the hydrological cycle in general circulation models.

Passive mm/sub-mm has some advantages compared to other space-borne cloud-ice remote sensing techniques. Solar reflectance and thermal infrared methods are inherently sensitive to optical depth, while mm/sub-mm radiometry is more directly sensitive to ice water path and particle size because the wavelengths are similar to the sizes of cirrus ice crystals. Visible and near infrared solar reflection methods(e.g., Rossow and Schiffer, 1999; Minnis et al., 1993; Rolland et al., 2000; Platnick et al., 2001) can't distinguish ice from underlying liquid water cloud, can't measure low optical depth clouds over brighter land surfaces, and only work during daytime. Solar techniques also retrieve an effective radius which is biased to the cloud top for thick clouds, and are highly sensitive to uncertainties in the nonspherical particle phase function (e.g. Mishchenko et al., 1996). Thermal infrared methods (e.g., Ou et al., 1995; Giraud et al., 1997; Stubenrauch et al., 1999) saturate for moderate optical depths and can only determine effective radius for small crystal sizes. 94 GHz Cloud profiling radar (e.g. Stephens et al., 2002) can penetrate very thick cirrus, but as with all single frequency techniques, it is susceptible to uncertainty in the particle size distribution. Another limitation is poor sampling from the lack of horizontal scanning ability. With multiple wavelengths chosen from the mm/sub-mm region it is possible to manage the penetration/sensitivity trade-off, while giving sensitivity to a broad enough range of the particle size distribution to constrain size distribution parameters and detect most of the cloud ice mass (e.g. Evans et al., 2002).

We define the cloud induced radiance as the difference between the observed radiance and that for the same atmosphere without clouds, $\Delta I = I_{\text{cloudy}} - I_{\text{clear}}$. A complicating

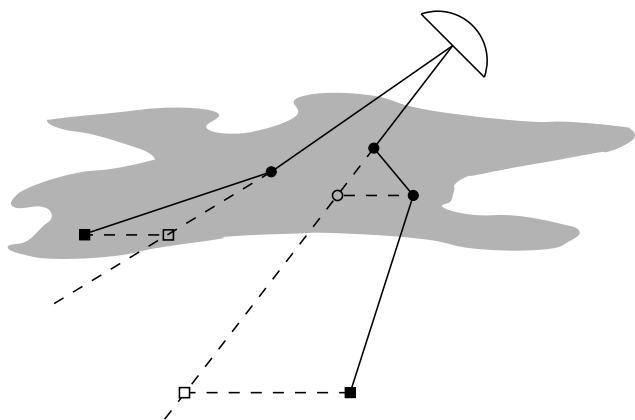*Correspondence to:* C. Davis
(cory.davis@metservice.com)

Fig. 1. A single-scattered and double-scattered photon path, with each incoming direction sampled from the antenna response function. The solid lines and dots show the 3-D RT procedure, where the dots show scattering events and the location of optical property look-up. For the IPA calculations optical properties are obtained from the original incoming ray shown by the open symbols.

factor in using mm/sub-mm wavelengths to observe cirrus, is that the particle/radiation interaction is dominated by scattering. For downlooking geometries, this tends to result in ice cloud decreasing the observed radiance, hence negative ΔI. For limb sounding the sign of ΔI can change from negative to positive with increasing tangent height. This sign change reflects the changing role of clouds in limb radiances from scattering radiation away from the line of sight to scattering radiation into the line of sight. This description, where scattering is the dominant process, is in contrast to the situation with liquid water clouds, and rainfall at low microwave frequencies, where the hydrometeors are mainly absorbing, and passive microwave observations over ocean yield a positive ΔI. Scattering complicates the radiative transfer (RT) part of the retrieval problem. Unlike clear sky remote sensing applications, where scalar RT without scattering can be applied and the solution is a simple path integral, the inclusion of scattering introduces polarisation and an influence from atmospheric properties outside the line of sight, and hence a requirement of 3-D geometry for a complete treatment. 3-D RT calculations are computationally demanding, and the field of 3-D RT is an area of considerable current research effort. Consequently, in remote sensing applications, where the speed of the "forward model" can be critical, 3-D polarised RT has not been used. Instead, the approximation of a 1-D plane-parallel atmosphere is often made, and polarisation is neglected.

In this work we use a state-of-the-art radiative transfer model (ARTS-MC), on a detailed midlatitude cirrus scenario, to give simulated observations for three different space-borne instruments: the Advanced Microwave Sounding Unit-B (AMSU-B) (e.g. Atkinson, 2001), the Cloud Ice Water Submillimetre Imaging Radiometer (CIWSIR) (Buehler, 2005),

and the Earth Observing System Microwave Limb Sounder (EOS-MLS) (Waters et al., 2006). As well as demonstrating the capability of the radiative transfer software to perform such detailed simulations, the results indicate the extent to which cloud inhomogeneity affects the radiances observed by these instruments, and the extent of polarisation effects caused by particle shape. The cloud-inhomogeneity and polarisation effects will have follow-on effects on cloud ice retrievals dependent on 1-D unpolarised forward models.

To identify any influence of cloud inhomogeneity, comparisons were made between 3-D RT and 1-D representations of the 3-D scenario. Any differences arising between 3-D and 1-D have two main causes: 1. FOV averaging over radiances that are in the large optical path/non-linear RT regime will cause a systematic bias compared to a 1-D representation with equivalent FOV averaged cloud optical path. 2. Actual 3-D radiative transfer effects resulting from photon transport perpendicular to the viewing direction through inhomogeneity not present in the 1-D representations. Effect 1 has been called beamfilling by previous authors, particularly with regard to passive microwave retrievals of rainfall rate (e.g. Wilheit et al., 1977; McCollum and Krajewski, 1998; Kummerow, 1998) and liquid water path in non-precipitating clouds (e.g. Lafont and Guillimet, 2004). To help attribute any observed 1-D/3-D difference to either beamfilling or 3-D radiative transfer effects, simulations were also performed using the Independent Pixel Approximation (IPA), which treats each incoming direction within the FOV as a unique 1-D RT calculation. Since, like the 3-D simulations, the IPA simulations also integrate over the FOV with the 3-D heterogeneous cloud field, the beamfilling effect will be observable. However the confinement of photons along a single path eliminates 3-D radiative transfer effects. Where there is good agreement between 3-D and IPA, yet significant differences between 3-D and 1-D, the beamfilling effect is dominant.

2 The models

All simulations were performed using the Monte Carlo scattering component of the Atmospheric Radiative Transfer Simulator (ARTS-1-1-*) software package, which we refer to as ARTS-MC. ARTS-MC includes the algorithm described by Davis et al. (2005a), which performs 3-D polarised radiative transfer for pencil-beam (infinitesimal solid angle) cases. More recently, a generalisation of this algorithm has been included, which allows for surface reflection and field of view (FOV) averaging. Naturally, the surface contributions and antenna pattern integration are performed using Monte Carlo integration (MCI) with importance sampling.

The purpose of the independent pixel approximation (IPA) RT calculations was to provide FOV averaged IPA calculations for comparison with 3-D RT to investigate the magnitude of true 3-D RT effects. IPA simulations were performed
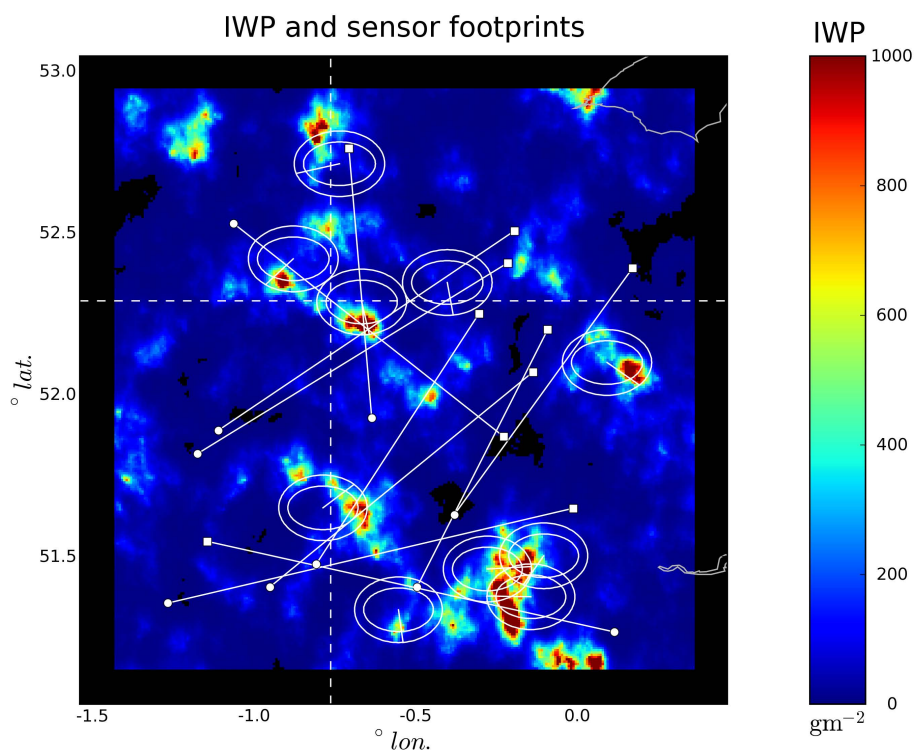
Fig. 2. Ice water path (IWP) for the 17 July 1999 cloudgen scenario. Approximate footprints for CIWSIR are shown as ellipses; along with the large AMSU footprint outside them. In each case the radial line points in the direction of the sensor. MLS views are shown by a line representing the bore-sight between the entry at the cloudtop (circle) and the exit at the cloud bottom (square). The two dashed lines show the position of the IWC slices potted in Fig. 3.

with a slightly modified version of the generalised Monte Carlo algorithm described above. The main point of difference lies in the looking-up of optical properties. As for the generalised Monte Carlo code, a reversed multiply scattered photon path is traced through the 3-D domain. However, the optical properties, which determine path length, scattering angle, and emission or scattering events, are obtained from the point on the original pencil beam viewing direction with the same pressure as the point in question. This is equivalent to each direction within the FOV being treated as an independent 1-D RT calculation. The difference between 3-D and IPA calculations is demonstrated in Fig. 1.

To avoid difficulties in comparing different models, the 1-D simulations were also performed using the 3-D Monte Carlo model, expanding a 1-D field (varying only with pressure) over the 3-D grid.

3 Scenario

3-D IWC fields were obtained from example output of Robin Hogan's cloudgen software (http://www.met.rdg.ac. uk/clouds/cloudgen/). This takes cloud radar data, in this case from the Chilbolton radar on 17 July 1999, and applies a stochastic method (Hogan and Kew, 2005) to generate a 3-D field from the 2-D (height, time) observations. Other required fields e.g. temperature, water vapour, height, were obtained from collocated ECMWF Operational Analysis data. The cloudgen grid was 256 by 256 by 64, corresponding to a resolution of approximately 780 m by 780 m by 110 m. This fine grid was merged with a coarser grid, wide enough to satisfy the condition that all photons not emitted in the atmosphere must enter either from the top of the atmosphere or the surface. Figure 2 shows the vertically integrated ice water path for the scenario. The non-zero IWC altitude range is 6.5–10.2 km. Example slices from the 3-D scenario are shown in Fig. 3.

To look at how polarisation responds to different particle aspect ratios or degrees of ice crystal horizontal alignment, we consider horizontally aligned oblate spheroids with aspect ratios 1.3 and 3.0. This range was chosen arbitrarily. The appropriate value for midlatitude cirrus is unknown due to a lack of dual polarised observations at these frequencies. Davis et al. (2005b) showed dual polarised EOSMLS 122 GHz ice cloud observations, which were consistent with simulations having particle aspect ratios of 1.2±0.15. However, the generality of this result is limited due to the frequency used; firstly, because O_2 absorption limited the observations to tropical ice cloud reaching over $\sim$9 km, and
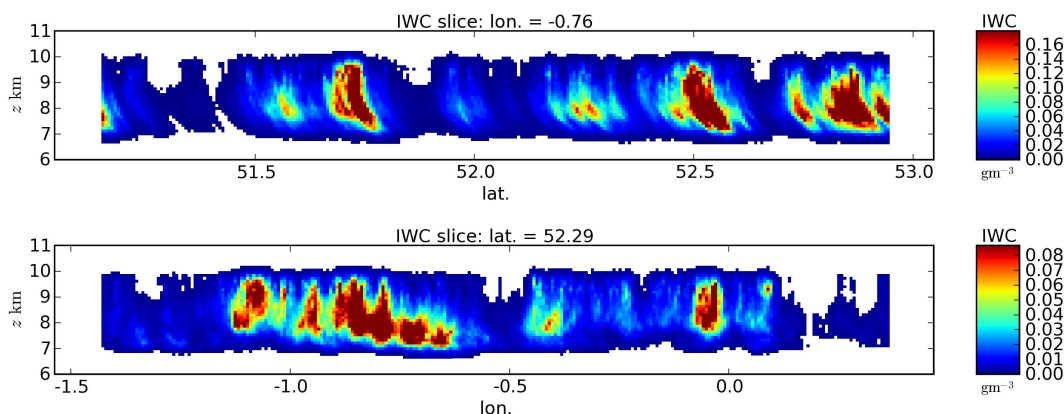
Fig. 3. A latitudinal and longitudinal IWC slice from the 3-D cloud ice scenario.

secondly the wavelength restricts sensitivity to only the larger ice particles. For the purpose of reproducing cloud induced radiance and polarisation signals, varying the aspect ratio of oblate spheroids is a reasonable proxy for the variation of shape and orientation distribution for realistic cirrus particles. For downlooking geometries, where the cloud signal is dominated by extinction, and the polarisation is dominated by dichroism, the important parameters are the K_{jj}, and K_{12} extinction matrix elements, which can be exactly specified by a choosing a horizontally aligned oblate spheroid with an appropriate size and aspect ratio. Optical properties were calculated using the PyARTS python package (http://www.met.ed.ac.uk/~cdavis/PyARTS), which incorporates the T-matrix code of Mishchenko (both fixed (Mishchenko, 2000) and random (Mishchenko and Travis, 1998) orientations). The McFarquhar and Heymsfield (1997) size distribution, which depends on IWC and temperature, was assumed, and non-spherical particles were related to the size distribution using volume equivalent radius.

While the micro-physical assumptions used here will produce optical properties able to reproduce actual observations in radiative transfer simulations, there is a large amount of uncertainty in the relationship between IWC and optical properties, caused by uncertainty in particle shape, density, and size distribution. While these are important issues in their own right, this paper focuses on the radiative transfer component of the forward modelling problem.

4   Instruments

In this study we simulated observations for 3 satellite borne passive instruments operating in the mm/sub-mm range. Two of these AMSU-B and EOSMLS, are designed to measure clear-sky atmospheric variables, with clouds mainly being an impediment to the focus measurements but with some cloud information produced as a secondary by-product. The

other instrument, CIWSIR, is a proposed instrument designed specifically for observing cloud ice.

The Advanced Microwave Sounding Unit -B (AMSU-B) is designed to allow the calculation of the vertical water vapour profiles. The instrument has full width half maximum (FWHM) of 1.1° and an altitude of 833 km. The antenna provides a cross-track scan, scanning 48.95° from nadir with a total of 90 Earth fields-of-view per scan line. For these simulations we have chosen Channel 20, which is the one most sensitive to cloud ice. The measurement is simulated by an RT calculation at only one frequency, 190.31 GHz, which is the central frequency of the upper pass-band of Channel 20. This is a good approximation of the real AMSU measurement.

CIWSIR (Cloud Ice Water Sub-millimetre Imaging Radiometer) is an instrument proposed for a recent ESA call for Earth Explorer Missions. This is a conical scanning radiometer with an earth incidence angle of 53°. 12 Channels are used to obtain sensitivity to a range of particle sizes such that the instrument is sensitive to a large majority of the ice mass within cirrus. For these simulations we choose example frequencies, 334.65 GHz, and 664 GHz. We consider the antenna to be 2-D Gaussian with FWHM of 0.377° and a sensor altitude of 833 km.

The Earth Observing System Microwave Limb Sounder (EOSMLS) is onboard the NASA Aura Satellite, which was launched on 15 July 2004. EOSMLS has radiometers at frequencies near 118, 190, 240, and 640 GHz and 2.5 THz. EOS MLS can observe cloud-induced radiances in all of these radiometers. The EOS-MLS IWC product uses cloud induced radiances from the 240 GHz radiometer. In these simulations we choose 230 GHz, which corresponds to a window channel in the lower side band. For the 240 GHz radiometer, the zenith FWHM is 0.061°, and the azimuth FWHM is 0.121°. The sensor altitude is 705 km. The 240 GHz radiometer measures only the H-polarised component of the limb radiance.

For each instrument 10 viewing positions/directions were chosen so as to span the available range of field of view

integrated ice water path, IWP$_{FOV}$. Figure 2 shows the approximate surface footprints for the simulations. For ease of comparison the AMSU and CIWSIR viewing positions and directions are the same. For MLS we consider 3 km tangent height observations. For these the viewing directions were restricted to those that entered through the the top of the cloudy region and exited though the bottom, avoiding the boundary of the non-zero IWC region. In each case the instrument antenna response function was 2-D Gaussian, with the zenith and azimuth full width half maximum (FHWM) corresponding to the instruments concerned.

5   Simulation details

The radiance error in all simulations is 0.2 K, with the exception of MLS, for which the error is 0.5 K. ΔI therefore has an error ($=\sqrt{\delta I_{\text{cloudy}}^2 + \delta I_{\text{clear}}^2}$) of 0.28 and 0.71 respectively. The Monte Carlo simulations use as many photons as is required to reach these accuracies. Consequently viewing directions with larger cloud optical path tend to have longer computing times. For the 3-D AMSU-B simulations the simulations took between 8 and 45 min on a single 3.2 GHz CPU. The CIWSIR simulations took between 17 and 70 min. The MLS simulations (0.5 K error) took between 11 and 32 min.

6   1-D representation

If we wish to investigate the effects of cloud inhomogeneity on microwave observations by comparing 3-D simulations with 1-D, we need to choose an appropriate method for representing the actual 3-D cloud structure in one dimension (in our case pressure). If radiative transfer is in the linear regime (low cloud optical path, τ_c), the 1-D and 3-D cases should give similar results if the FOV averaged τ_c is the same for 1-D and 3-D cases. Therefore, the goal when producing 1-D scenarios for comparison with 3-D simulations, is to provide 1-D scenarios with equal field of view averaged cloud optical path $\bar{\tau}_c$. The calculation of $\bar{\tau}_c$ can be transformed to a volume integration over radius (r), latitude (δ), and longitude (λ) coordinates, and thereby expediting its numerical computation in the ARTS pressure, latitude, longitude grid system.

$$\bar{\tau}_c = \int_{\text{FOV}} a\tau_c d\Omega$$
$$= \int_{\text{FOV}} \int aK_{11}dsd\Omega, \tag{1}$$

where K_{11} is the (1,1) element of the extinction matrix, which is summed over all particle sizes, shapes, and orientations, $d\Omega$ is an element of solid angle, and a is the normalised antenna response function. If we recognise that this is almost a volume integral, with volume element

$$dV = s^2 dsd\Omega = r^2 \cos(\delta)drd\delta d\lambda, \tag{2}$$

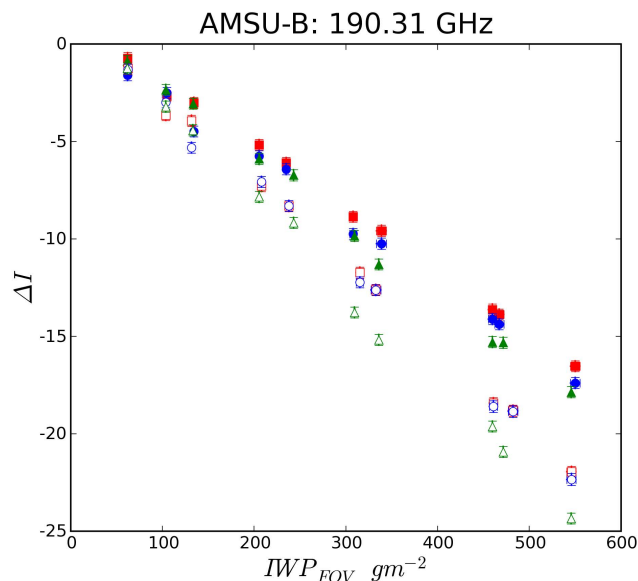**Fig. 4.** Simulation ΔI results for AMSU-B. Results are shown for full 3-D RT (red squares), the independent pixel approximation (blue circles), and a 1-D representation (green triangles) for each viewing position. The solid symbols refer to the 1.3 aspect ratio (AR) results, and the hollow symbols are for AR=3.0

where s is the distance from the sensor and r is the distance from the earth centre, we get

$$\bar{\tau}_c = \int \int \int \frac{r^2}{s^2} aK_{11} \cos(\delta)drd\delta d\lambda$$
$$= -\frac{R}{g} \int \int \int \frac{r^2}{s^2} aK_{11} \cos(\delta)Td\log pd\delta d\lambda, \tag{3}$$

where we have used the hydrostatic equation to replace the radius coordinate with $\log p$. T and p are the thermodynamic temperature and pressure respectively, g and R are the gravitational and gas constants respectively. The limits of integration are the pressure, latitude, and longitude bounds of the cloud field. K_{11} is represented as the sum of products of particle number densities N_i and K_{11}^i for a finite number of particle sizes. From Eq. (3), the following expression for averaging number densities for each particle size over each constant pressure surface will result in $\bar{\tau}_c$ equal to the 3-D case.

$$N_i^{1D(p)} = \frac{\int \int \frac{r^2}{s^2} aN_i^{(p)} \cos(\delta)Td\delta d\lambda}{\int \int \frac{r^2}{s^2} a \cos(\delta)Td\delta d\lambda} \tag{4}$$

7   Results

For AMSU-B the cloud optical path is smaller than for the CIWSIR and MLS simulations presented here. Radiative transfer is therefore in the linear regime, which is apparent in
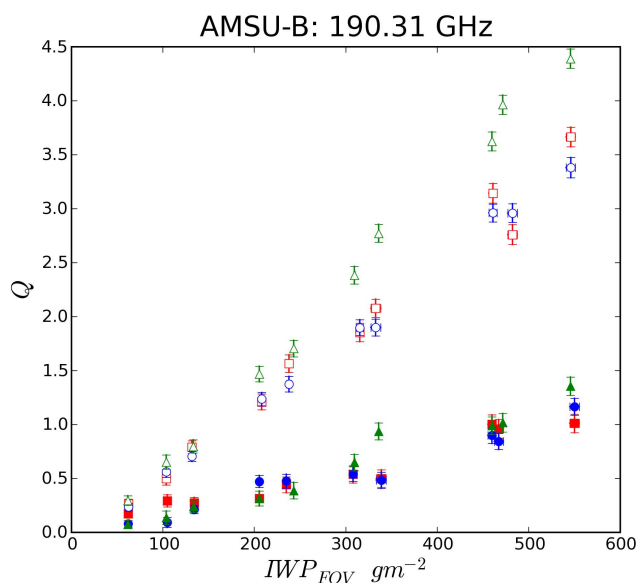
Fig. 5. Simulation Q results for AMSU-B. Symbol definitions as for Fig. 4.

Fig. 6. Simulation ΔI results for CIWSIR 334.65 GHz.

the ΔI values in Fig. 4. ΔI for the 3-D and IPA simulations are all very close, for AR=1.3 1-D is also very close to 3-D and IPA. The AR=3 particles have an increased extinction cross-section when viewed from above, therefore ΔI has a larger magnitude. For AR=3 a difference between 1-D and 3-D radiative transfer becomes increasingly apparent. The polarisation signal Q has a small signal that is linear with IWP$_{FOV}$ (Fig. 5), with a larger slope for the AR=3. Again for AR=3, the 1-D representation begins to depart significantly from 3-D and IPA results as IWP increases. Again there is no significant difference between 3-D and IPA.

The smaller wavelength for CIWSIR results in a larger scattering cross-section and we see the radiative transfer move into the non-linear regime. For the 334.65 GHz channel we see, for IWP$_{FOV}$ <400 gm^{-2}, ΔI varying linearly with IWP$_{FOV}$ (Fig. 6), and for the higher values there is saturation, with ΔI no longer increasing with IWP$_{FOV}$. For 664 GHz this transition occurs at a lower IWP$_{FOV}$ (Fig. 8). Again due to the higher scattering cross section for the more aspherical particles, the AR=3 case gives a larger cloud signal for a given IWP$_{FOV}$. In all cases the IPA and 3-D ΔI values are very close. Again, as IWP$_{FOV}$ increases the 1-D representation increasingly over-predicts the magnitude of the cloud signal. Again the increase in aspect ratio from 1.3 to 3 causes a dramatic increase in the polarisation difference Q (Figs. 7 and 9). As for ΔI, the transition between the linear and non-linear regime is apparent, and again at a lower IWP$_{FOV}$ for 664 GHz. Again the 3-D and IPA results are relatively consistent. For the AR=3, 334.65 GHz, simulations the 1-D representation consistently over-predicts the magnitude of the polarisation signal by an amount that reaches a maximum somewhere between 400 and 600 gm^{-2}. For the
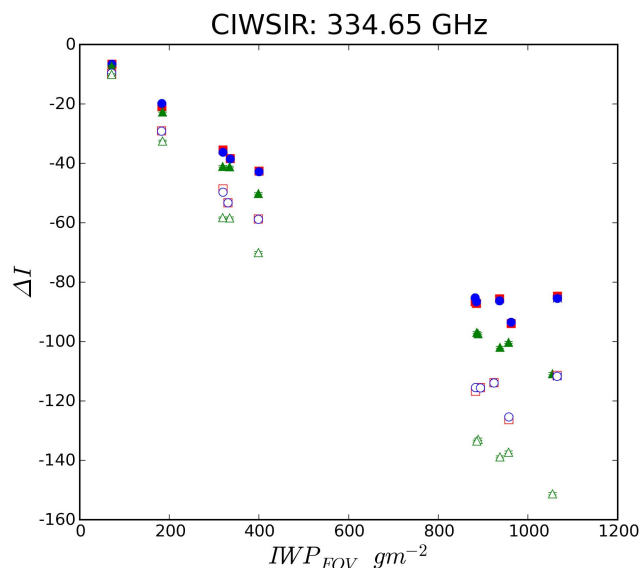
more optically thick 664 GHz simulations this 1-D-3-D difference actually changes sign for high IWP$_{FOV}$.

The MLS ΔI results (Fig. 10) are qualitatively similar to the 334 GHz CIWSIR results. We are seeing the transition to the non-linear regime for the higher values of IWP$_{FOV}$, the 3-D and IPA results are very similar, and the 1-D representation over predicts the cloud signal by up to 20K for high IWP$_{FOV}$. One difference is that the change in ΔI between AR=1.3 and 3 is less pronounced as for CIWSIR, the crystals having similar scattering cross-sections when viewed side on. The polarisation signal and its variation with IWP$_{FOV}$ (Fig. 9) is also qualitatively similar to the CIWSIR 334 GHz results. There is a significant polarisation signal for AR=3, good agreement between 3-D and IPA, and an overestimate for 1-D that has a maximum. The 240 GHz radiometer measures only the H-polarised component of the limb radiance, therefore the calibrated Level 1B radiances are actually given by $I-Q$, and therefore the cloud signal is $\Delta T_H = \Delta I - Q$, which is plotted in Fig. 12. This shows that such observations will be sensitive to changes in particle aspect ratio.

8 Discussion

8.1 The Beamfilling Effect

The differences between 3-D and 1-D simulations for the slant viewing instruments, CIWSIR and AMSU-B, and also for low tangent height EOSMLS, increase with increasing FOV averaged cloud optical path $\bar{\tau}_c$.

As $\bar{\tau}_c$ increases two possible mechanisms begin to differentiate 3-D and 1-D simulations. Firstly, averaging over inhomogeneities in the field of view, where some parts of the field of view have high enough optical path to be in the
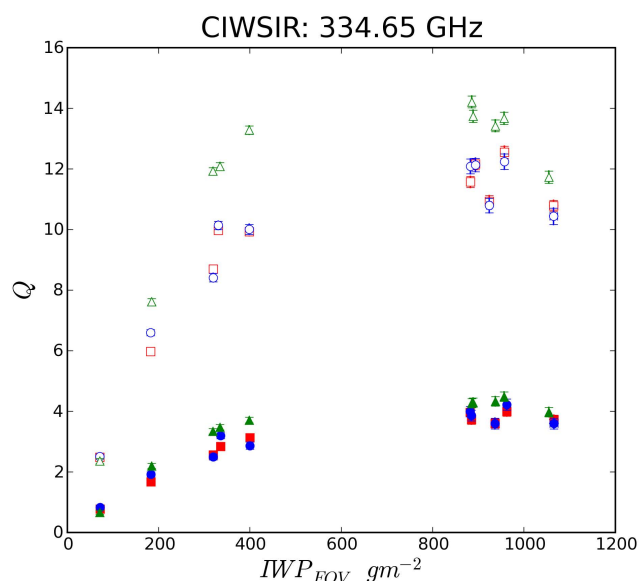
Fig. 7. Simulation Q results for CIWSIR 334.65 GHz.

Fig. 8. Simulation ΔI results for CIWSIR 664 GHz.

non-linear radiative transfer regime, will cause 3-D scenarios to produce smaller ΔI and Q than 1-D representations with equal $\bar{\tau}_c$. This has been called the beamfilling effect in the literature describing passive microwave remote sensing of rainfall rate. Secondly there are 3-D radiative transfer effects due to scattering perpendicular to the bore sight path.

The observed behaviour of increasing systematic 1-D/3-D differences is consistent with the beamfilling effect. The lack of any significant differences between 3-D and IPA results indicates that 3-D radiative transfer effects are negligible.

In passive microwave retrievals of rain rate, the assumption of homogeneous rainfall across the FOV, coupled with the non-linear, concave downwards, response of brightness temperatures to rainfall rate, leads to underestimates in the retrieved rainfall. This effect has been called beamfilling (Kummerow, 1998; McCollum and Krajewski, 1998; Lafont and Guillimet, 2004). The beamfilling effect was found to be the main source of error in retrieved rainfall rate; a factor of 2 can exist in the mean rain-rate for a given brightness temperature (Wilheit et al., 1977; Lafont and Guillimet, 2004). The beamfilling effect depends mainly on cloud type, and also on cloud shape, and in all case increases with inhomogeneity and mean LWP or rain-rate (Lafont and Guillimet, 2004). The beamfilling effect obviously depends also on the footprint dimension and the frequency under investigation. The effect of cloud ice on observed brightness temperature differs from that for rain drops and liquid water cloud because of the complex refractive index and size of the hydrometeors concerned, and also the cloud altitude. Cloud liquid water droplets and raindrops have a high imaginary part of the refractive index, and hence their effect is that of enhanced atmospheric absorption (emission). When viewed
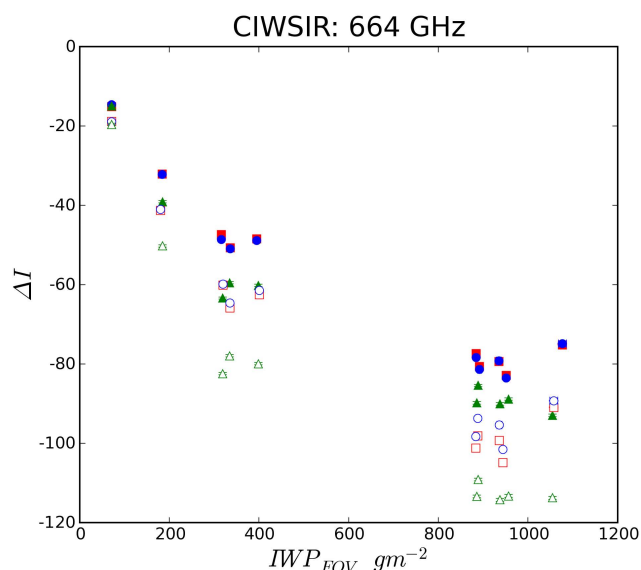
over the radiometrically cold ocean, rain and liquid water clouds produce an increased brightness temperature compared with a clear sky. On the other hand cloud ice crystals have only a small imaginary part for the refractive index and particle sizes up to several millimetres, so their effect on brightness temperature is dominated by scattering. In down-looking cases this results in a brightness temperature depression, as radiation from the warmer lower atmosphere is scattered away from the line of sight. Therefore the sign of the cloud signal is reversed from the rainfall/liquid water cloud case. However, like the rainfall and liquid water cloud cases, the magnitude of the cloud signal varies non-linearly (concave-down) with the amount of water in the FOV. This is due to the familiar "saturation" effect, as the cloud becomes opaque at increased IWP. So with increasing FOV averaged IWP, and increasing inhomogeneity, we might expect beam filling errors in ice cloud observations to become significant. One difference we might expect for ice clouds due to the increased role of scattering is that 3-D radiative transfer effects would be more pronounced than for rainfall or liquid water clouds.

We now present a simple mathematical description of the beamfilling effect, which explains the observed differences between 3-D and 1-D representations. We consider the pencil beam cloud induced radiance to be primarily a function of the pencil beam cloud optical path. Here we are considering a downlooking ice cloud observation, where ΔI is negative. For convenience we drop the sign and consider ΔI to be the magnitude of the cloud signal.

$$\Delta I \approx \Delta I(\tau_c) \qquad (5)$$

For low optical path, this relationship is almost linear, but due to saturation the curve levels off with increasing optical
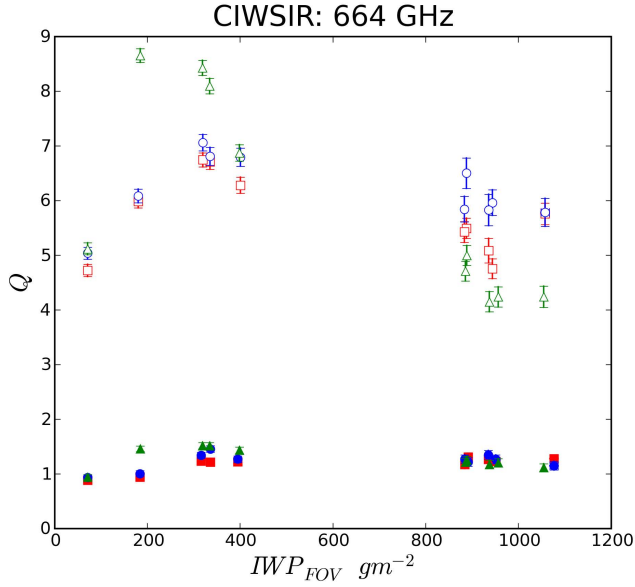
Fig. 9. Simulation Q results for CIWSIR 664 GHz.

Fig. 10. Simulation ΔI results for MLS.

path, i.e.:

$$\frac{d^2 \Delta I}{d\tau_c^2} < 0 \tag{6}$$

If we take a Taylor series expansion of the cloud induced radiance about the field of view averaged cloud optical path, $\bar{\tau}_c$ we get the following expression for an actual observation of cloud induced radiance convolved with antenna response function, a.

$$\int_{\text{FOV}} a \Delta I d\Omega \approx$$

$$\int_{\text{FOV}} a \left[\Delta I (\bar{\tau}_c) + \left(\frac{d\Delta I}{d\tau_c} \right)_{\bar{\tau}_c} (\tau_c - \bar{\tau}_c) + \right.$$

$$\left. \frac{1}{2} \left(\frac{d^2 \Delta I}{d\tau_c^2} \right)_{\bar{\tau}_c} (\tau_c - \bar{\tau}_c)^2 \right] d\Omega$$

$$= \Delta I (\bar{\tau}_c) + \frac{1}{2} \left(\frac{d^2 \Delta I}{d\tau_c^2} \right)_{\bar{\tau}_c} \int_{\text{FOV}} a (\tau_c - \bar{\tau}_c)^2 d\Omega$$

$$= \Delta I (\bar{\tau}_c) + \frac{1}{2} \left(\frac{d^2 \Delta I}{d\tau_c^2} \right)_{\bar{\tau}_c} \sigma_{\tau_c}^2 \tag{7}$$

$$< \Delta I (\bar{\tau}_c),$$

where $\sigma_{\tau_c}^2$ is the variance in cloud optical depth sampled according to the antenna response function. This gives a first order description of the beamfilling effect as apparent in the divergent 1-D and 3-D curves in Figs. 4–12. We have chosen τ_c as the independent variable here because what we are seeing is a radiative transfer effect, which is most easily understood in terms of τ_c. The same analysis could also be performed using IWP$_{\text{FOV}}$ as the independent variable.
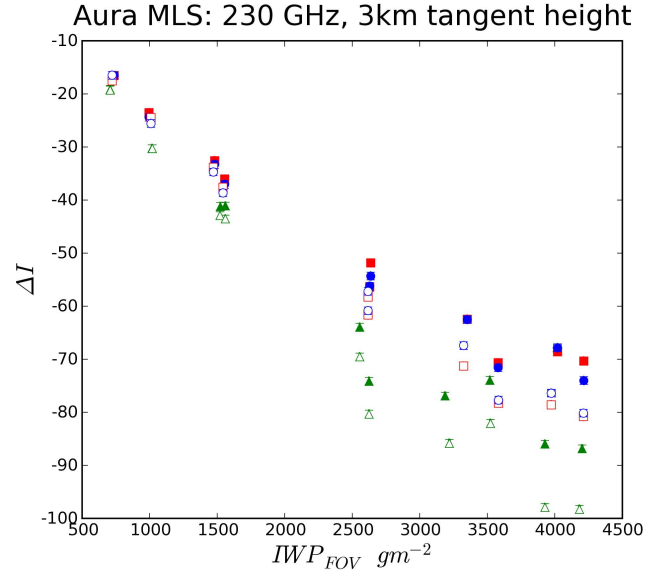
These results suggest that CIWSIR, EOSMLS, and to a lesser extent AMSU-B ice cloud observations could be adversely affected by beamfilling. Mitigation of this effect would require a dedicated simulation study. Lafont and Guillimet (2004) found that for microwave rainfall and LWP retrievals, the beam filling effect can be corrected by a simple factor based on sub-pixel cloud cover which could be obtained from collocated visible measurements. With this in mind, a possible beamfilling error mitigation for MLS ice cloud observations would be to utilise other A-train cloud observations, such as those from MODIS and CloudSat, to estimate sub-pixel inhomogeneity and hence the beamfilling error.

As here, Kummerow (1998) demonstrated that for rainfall observations, 3-D radiative transfer effects were small, rarely exceeding a few degrees. Given the increased role of scattering in ice observations we might expect 3-D RT effects to be bigger. This was not the case in these simulations. A possible explanation for this is that 3-D RT effects produce both positive and negative effects on pencil beam radiances, which cancel one another out when integrated over the FOV. As was also noted by Kummerow (1998), the lack of 3-D RT effects may not apply where the cloud systems are smaller than the field of view, for example tropical convective clouds.

8.2 Polarisation and the beamfilling effect

For the slant viewing and low tangent height limb sounding, the positive Q values (and hence partial vertical polarisation) can be described as dichroism. The horizontally polarised component of the upwelling radiation is attenuated by horizontally aligned particles more than the vertically polarised component. The differences in polarisation behaviour
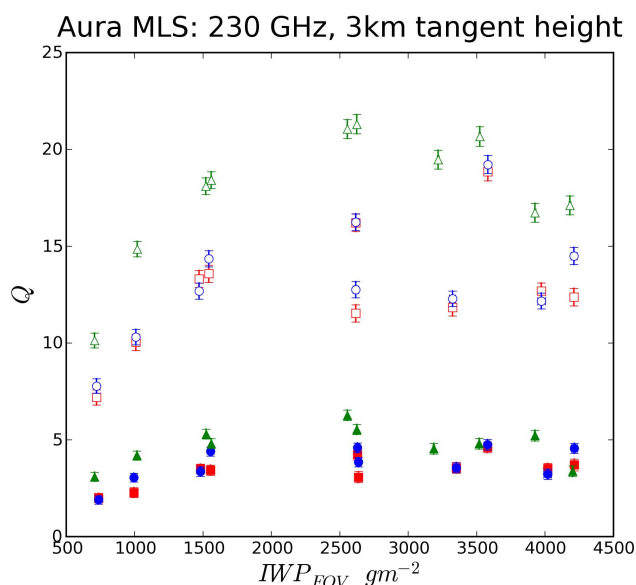
Fig. 11. Simulation Q results for MLS.

Fig. 12. $\Delta T_H = \Delta I - Q$ results for MLS.

between 1-D and 3-D simulations is due to the same mechanism as for the 3-D/1-D ΔI differences: the beamfilling effect. As for ΔI, Q is very similar for the 3-D and IPA simulations. For a given aspect ratio, the variation in Q with respect to optical path for down-looking cases is also non-linear concave-down with respect to optical path. Therefore averaging Q over the FOV, where parts of the FOV are in the non-linear radiances regime will also cause systematic differences between 3-D and 1-D representations. It can be shown that at even higher cloud optical path, the polarisation signal Q will decrease from its maximum and level off to a constant value. This results in a concave-up region where the second derivative is positive and hence a reversal in sign for the beamfilling effect. In this work this is seen only in the 664 GHz CIWSIR simulations.

9 Conclusions

This paper presents detailed 3-D polarised simulations of space-borne mm/sub-mm cirrus observations. These simulations confirm that the aspect ratio and degree of horizontal orientation of ice crystals will have a significant impact on slant viewing and limb sounding observations. Aspect ratios can also have a noticeable effect on the brightness temperature depression, particularly for high tangent height MLS observations.

For all instruments there are significant differences between 1-D and 3-D results, but generally good agreement between 3-D and IPA. For the the slant looking instruments and for low tangent height limb sounding observations, the 1-D/3-D difference is systematic, with 1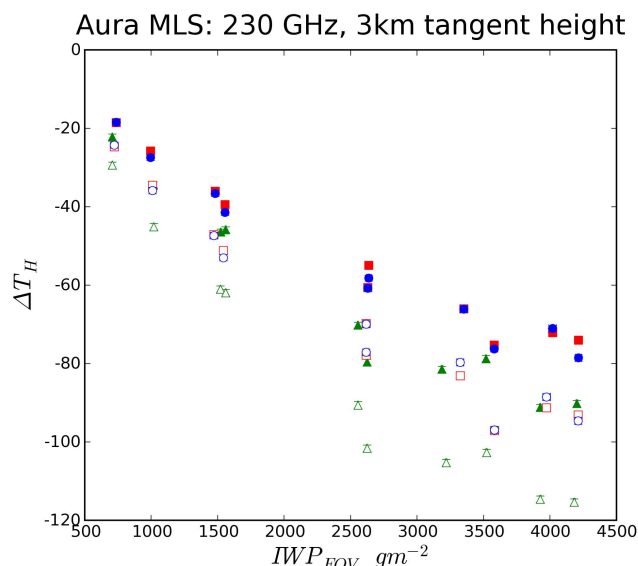-D representations over-estimating the magnitude of both ΔI and Q by an amount that increases with the magnitude of ΔI and hence the cloud optical path. Agreement between 3-D and IPA simulations suggests that for slant viewing instruments and low tangent height limb sounding, 3-D radiative transfer effects did not have a significant impact in these cases. We have demonstrated that in these cases the 1-D/3-D differences were a result of the beamfilling effect – a straightforward consequence of averaging over non-linear radiances.

A contribution of actual 3-D radiative transfer effects has not been found in these few instances, but it is premature to rule them out on this basis. Similarly, a more complete quantification of the beamfilling effect and polarisation for a given instrument requires a dedicated separate study involving many midlatitude and tropical cloud scenes, and many more viewing directions. Such work was intentionally beyond the scope of this paper, but planned for the future.

References

Atkinson, N. C.: Calibration, monitoring and validation of AMSU-B, Adv. Space Res., 28(1), 117–126, 2001.

Buehler, S. A.: Cloud Ice Water Submillimeter Imaging Radiometer (CIWSIR) Mission Proposal, http://www.sat.uni-bremen.de/projects/ciwsir/cirrus_expl_2005_09_05.pdf, 2005.

Davis, C., Emde, C., and Harwood, R.: A 3D Polarized Reversed Monte Carlo Radiative Transfer Model for mm and sub-mm Passive Remote Sensing in Cloudy Atmospheres, IEEE Trans. Geosci. Remote Sensing, 43, 1096–1101, 2005a.

Davis, C. P., Wu, D. L., Emde, C., Jiang, J. H., Cofield, R. E., and Harwood, R. S.: Cirrus Induced Polarization in 122 GHz Aura Microwave Limb Sounder Radiances, Geophys. Res. Lett, 32, L14806, doi:10.1029/2005GL022681, 2005b.

Evans, K. F., Walter, S. J., Heymsfield, A. J., and McFarquhar, G. M.: Submillimeter-Wave Cloud Ice Radiometer: Simulations of retrieval algorithm performance, J. Geophys. Res., 107(D3), 4028, doi:10.1029/2001JD000709, 2002.

Giraud, V., Buriez, J. C., Fouquart, Y., Parol, F., and Seze, G.: Large-scale analysis of cirrus clouds from AVHRR data: Assessment of both a microphysical index and the cloud-top temperature, J. Appl. Met., 36, 664–675, 1997.

Hogan, R. J. and Kew, S. F.: A 3D stochastic cloud model for investigating the radiative properties of inhomogeneous cirrus clouds, Q. J. R. Meteorol. Soc., 131, 2585–2608, 2005.

Houghton, J., Ding, Y., Griggs, D., Noguer, M., van der Linden, P., Dai, X., Maskell, K., and Johnson, C. A. (Eds.): IPCC, 2001: Climate Change 2001: The Scientific Basis, Contribution of Working Group I to the Third Assessment Report of the Intergovernmental Panel on Climate Change, Cambridge University Press, 2001.

Kummerow, C.: Beamfilling Errors in Passive Microwave Rainfall Retrievals, J. Appl. Meteorol., 37, 356–370, 1998.

Lafont, D. and Guillimet, B.: Subpixel fractional cloud cover and inhomogenety effects in microwave beam filling error, Atmos. Res., 72, 149–168, 2004.

Lynch, D., Sassen, K., Starr, D. O., and Stephens, G.: Cirrus, Oxford University Press, 2002.

McCollum, J. and Krajewski, W.: Investigations of error sources of the Global Precipitation Climatology Project emission algorithm, J. Geophys. Res., 103, 28711–28719, 1998.

McFarquhar, G. and Heymsfield, A.: Parametrization of tropical ice crystal size distributions and implications for radiative transfer: Results from CEPEX, J. Atmos. Sci., 54, 2187–2200, 1997.

Minnis, P., Heck, P. W., and Young, D. F.: Inference of cirrus cloud properties using satellite-observed visible and infrared radiances. Part II: Verification of theoretical cirrus radiative properties, J. Atmos. Sci., 50, 1305–1322, 1993.

Mishchenko, M.: Calculation of the amplitude matrix for a non-spherical particle in a fixed orientation, Appl. Opt., 39, 1026–1031, 2000.

Mishchenko, M. I., Rossow, W. B., Macke, A., and Lacis, A. A.: Sensitivity of cirrus cloud albedo, bidirectional reflectance and optical thickness retrieval accuracy to ice particle shape, J. Geophys. Res., 101(D12), 16973–16986, doi:10.1029/96JD01155, 1996.

Mishchenko, M. and Travis, L.: Capabilities and limitations of a current FORTRAN implementation of the T-matrix method for randomly oriented, rotationally symmetric scatterers, J. Quant. Spectrosc. Radiat. Transfer, 60, 309–324, 1998.

Ou, S. C., Liou, K. N., Takano, Y., Rao, N. X., Fu, Q., Heymsfield, A. J., Miloshevich, L. M., Baum, B., and Kinne, S. A.: Remote sounding of cirrus cloud optical depths and ice crystal sizes from AVHRR data: Verification using FIRE II IFO measurements, J. Atmos. Sci., 52, 4143–4158, 1995.

Platnick, S., Li, J. Y., King, M. D., Gerber, H., and Hobbs, P. V.: A solar reflectance method for retrieving the optical thickness and droplet size of liquid water clouds over snow and ice surfaces, J. Geophys. Res., 106(D14), 15185–15199, 2001.

Rolland, P., Liou, K. N., King, M. D., Tsay, S. C., and McFarquhar, G. M.: Remote sensing of optical and microphysical properties of cirrus clouds using Moderate-Resolution Imaging Spectroradiometer channels: Methodology and sensitivity to physical assumptions, J. Geophys. Res., 105, 11721–11738, 2000.

Rossow, W. B. and Schiffer, R. A.: Advances in understanding clouds from ISSCP, Bull. Amer. Meteor. Soc., 80, 2261–2287, 1999.

Stephens, G. L., Vane, D. G., Boain, R. J., Mace, G. G., Sassen, K., Wang, Z., Illingworth, A. J., O'Connor, E. J., Rossow, W. B., Durden, S. L., Miller, S. D., Austin, R. T., Benedetti, A., Mitrescu, C., and CloudSat Science Team: The CloudSat mission and the A-train: A new dimension of space-based observations of clouds and precipitation, Bull. Amer. Meteor. Soc., 83, 1771–1790, doi:10.1175/BAMS-83-12-1771, 2002.

Stubenrauch, C., Holz, R., Chedin, A., Mitchell, D. L., and Baran, A. J.: Retrieval of cirrus ice crystal sizes from 8.3 and 11.1 micron emissivities determined by the improved initialization inversion of TIROS-N Opertional Vertical Sounder observations, J. Geophys. Res., 104, 793–808, 1999.

Waters, J. W., Froidevaux, L., Harwood, R. S., et al.: The Earth Observing System Microwave Limb Sounder (EOS MLS) on the Aura satellite, IEEE Trans. Geosci. Remote Sensing, 44(5), 1075–1092, 2006.

Wilheit, T., Chang, A., Rao, M., Rodgers, E., and Theon, J.: A satellite technique for quantitatively mapping rainfall rates oer the oceans, J. Appl. Meteorol., 16, 551–560, 1977.